Electron-Cloud Simulations: Build Up and Related Effects*

G. Rumolo and F. Zimmermann, CERN, Geneva, Switzerland

Abstract

ECLOUD is a simulation programme developed at CERN
which models the process of build up of an electron cloud
inside the vacuum chamber for proton or positron beams,
which is due to a primary source (photoemission or residual
gas ionization) and secondary emission. The main ingre-
dients of the code are described here with special empha-
sis on the physical modeling of processes like secondary
emission and elastic reflection of the electrons at the pipe
walls. Electron energy spectra, heat load on the LHC beam
screen, spatial patterns of the electron cloud, electron flux
at pick-up buttons, multi-bunch instability growth rates,
electron trapping by magnetic fields, and electron-cloud
build up for electron beams can also be studied using these
simulations.

1 INTRODUCTION

This paper consists of two parts. In the first, we describe
the simulation model, including the treatment of photoe-
mission, secondary emission, magnetic fields, beam fields,
image charges, and electron space charge. In the second
part, we present example simulation results, such as a com-
parison of multipacting thresholds in a dipole field and in a
field-free region (for the SPS), the electron-cloud build up
for the SPS fixed-target beam, the electron signal detected
by LHC button pick ups, growth rates for the multibunch
instability in the LHC, the spatial structure of the electron
cloud in dipole and quadrupole magnets, the probability
of electron trapping in a quadrupole field (for the KEKB
LER), and the electron-cloud build up for an electron beam
(KEKB HER).

2 SIMULATION CODE

2.1 General Remarks

The programme ECLOUD models the build up of the elec-
tron cloud during the passage of a bunch train. Its first
version was written at CERN in 1997 [1]. Since then con-
tinually extended, updated, and improved [2, 3, 4, 5, 6]. A
preliminary user guide is available [7]. The code can be
downloaded from the CERN electron-cloud web site [8].

The basic layout of the ECLOUD programme is similar
to the code PEI, developed by K. Ohmi at KEK in 1995,
and to POSINST, written by M. Furman and G. Lambertson

at LBNL since 1995 [9, 10]. Other codes modelling elec-
tron cloud build up are due to T.-S. Wang (LANL), L. Wang
(KEK), Z. Guo (IHEP), and M. Blaskiewicz (BNL).

We will illustrate the main features of ECLOUD and typ-
ical simulation results presenting various applications to
the LHC, SPS, and KEKB. A table with pertinent beam
parameters for these machines can be found in Ref. [11]. A
companion paper reports further results for the LHC [12].

2.2 Simulation Recipe

The simulation recipe of ECLOUD is illustrated by the
schematic in Fig. 1. The main ingredients have been de-
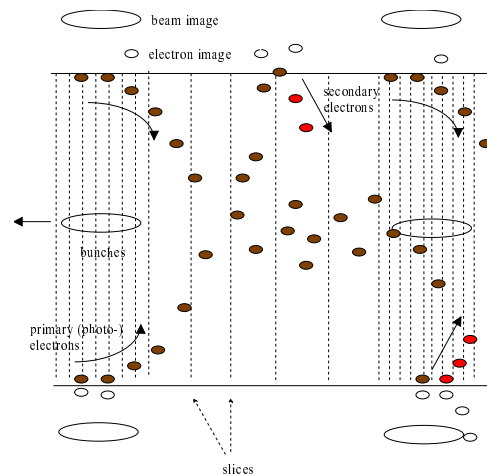scribed in Refs. [4, 5, 6].

Figure 1: Schematic of simulation recipe.

A certain section of the vacuum chamber, typically 1 m
long, is simulated. The magnetic field in this region is spec-
ified as an input.

The primary electrons, which are created by photoemis-
sion or beam loss on the wall, or due to ionization inside the
beam volume, are represented by macro-electrons, whose
charge is (much) larger than the charge of a real electron.

Both the bunches and the gap between bunches are sliced
into segments, of the order of 50–200 each. The slices in-
side the bunch are usually choosen shorter than those in the
gap, in order to accurately model the motion of the elec-
tron under the strong accelerating field of the beam. For
each bunch slice a certain number of macro-electrons are
generated, and existing macro-electrons are propagated in
the field of the bunch (and external magnetic fields, etc.).
Typically, per passing bunch a total of 1000–2000 macro-
electrons are launched on the wall, or inside the beam.

The electron motion is computed in 3 dimensions. The boundary conditions are effectively periodic in z. In addition to the beam field and the magnetic fields, also the electron space-charge field, beam-image charges and electron image fields are taken into account. The electron space-charge field is important, as without it the electron cloud build up would continue indefinitely. The space charge of the electrons causes a saturation of the build up at an electron cloud density close to the average neutralization density, for which the average electric field on the wall is zero. Image charges are important if the chamber is not round, if the beam orbit is offset from the center of the beam pipe, or if the electron cloud is not uniform (*e.g.*, in a dipole magnet).

Whenever a macro-electron hits the wall, it is remitted at the same location as (either true or elastically reflected) secondary electron and its charge is changed according to the value of the secondary emission yield computed as a function of its energy and its angle of incidence. This is a difference to the code POSINST where all macro-electrons have identical charge.

Between bunches the macro-electrons only experience the magnetic field, and the direct and image fields of the electron cloud itself. The latter two are approximated either by discrete kicks, applied after each slice, or by a continuous constant acceleration over the length of the slice.

The LHC chamber cross section is a circle that is vertically cut off, as shown in Fig. 2. When computing particle loss or launching new particles we use the actual boundary (the solid line in the figure). For the image-charge calculation we approximate the geometry by the inscribed ellipse, making use of an analytical expression for the image charge with elliptical boundary (see below).
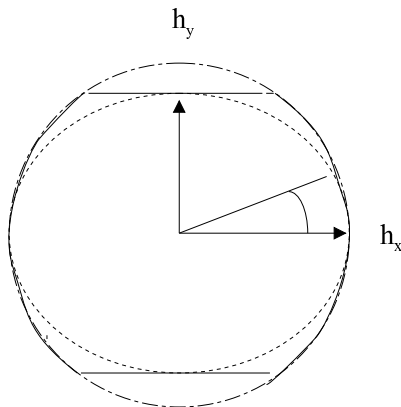

Figure 2: Transverse aperture in the LHC arcs. The solid line describes the actual cross section of the LHC beam screen.

2.3 Photoemission

The photoemission is characterized by 3 input variables: (1) the number of photons emitted per meter and per beam particle, (2) the photon reflectivity R, and (3) the azimuthal distribution of the reflected photons.

If $R = 0$, all photoelectrons are emitted from the horizontally outward side of the chamber, constrained to a cone with rms angle ϕ of order $1/\gamma$. If $R > 0$, a fraction R of the photoelectrons is launched at other azimuthal angles ϕ around the wall of the chamber. Figure 3 shows two initial distributions of the photo-electron starting positions as a functon of the transverse azimuthal angle ϕ. The two distributions depicted correspond to $R = 10\%$ and $R = 100\%$, respectively, and to an approximately uniform reflection. This example refers to the LHC chamber; a small distortion is caused by the vertical chamber cut off.
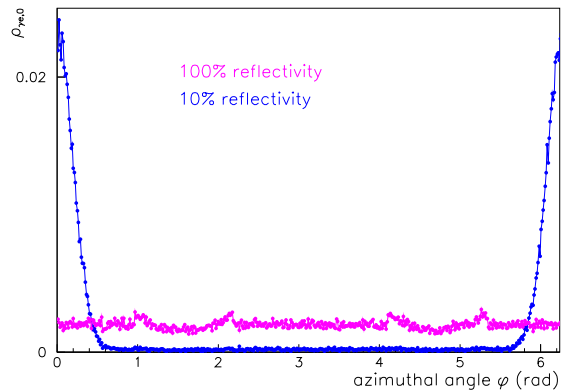

Figure 3: Initial azimuthal distribution of photoelectrons for 10% and 100% photon reflectivity.

Figure 4 defines the photon reflection angle θ. Measurements in Russia have shown that, for the LHC sawtooth chamber, the distribution of the diffusely reflected photons is not uniform, but consistent with a $\cos^2 \theta$ distribution [13].
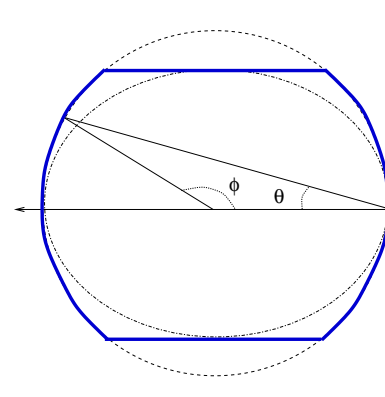

Figure 4: Definition of angles ϕ and θ.

Various distributions for the photoelectrons are compared in Fig. 5. They can be selected as input to the pro-

gramme. The dependence of the LHC heat load on the photon distribution was studied in Ref. [5].

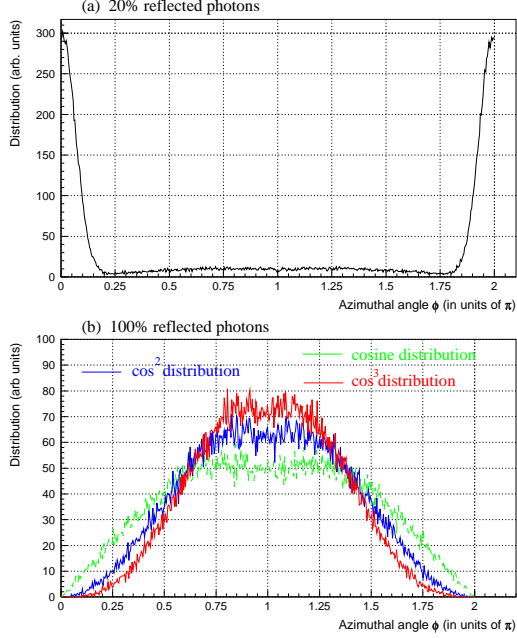(a) 20% reflected photons

(b) 100% reflected photons

Figure 5: Initial azimuthal distribution of photoelectrons for (a) 20% and (b) 100% photon reflectivity, considering different distributions [5].

After determining the launch points of the primary photo-electrons, we now address their initial velocity. The initial angular velocity distribution of the newly generated primary electrons is assumed to be uniform in the two spherical coordinates $\tilde{\theta}$ and $\tilde{\phi}$, which are defined with respect to the local surface normal (note that these angles $\tilde{\phi}$ and $\tilde{\theta}$ refer to the azimuthal and polar angles in the local coordinate system at the point of electron emission; they are different from the angles θ and ϕ mentioned above). The energy distribution of the emitted photoelectrons is modelled as a truncated Gaussian centered at 7 eV, with a standard deviation of 5 eV.

Figure 6 displays the initial energy distribution of the photoelectrons as well as the distribution after the first bunch passage, for an LHC dipole.

2.4 Magnetic Field

Standard possibilities include field-free region, strong or weak dipole, quadrupole, or solenoid. All these fields may vary with longitudinal position z. More generally, an arbitrary field can be calculated, as long as it is expressed in analytical form.

As an example, in a paraxial approximation the magnetic field components for a periodic series of solenoids are

$$B_x(x,y,z) \quad = \quad -\frac{1}{2}B_0 kx \cos kz \qquad (1)$$

$$B_y(x,y,z) \quad = \quad -\frac{1}{2}B_0 ky \cos kz$$

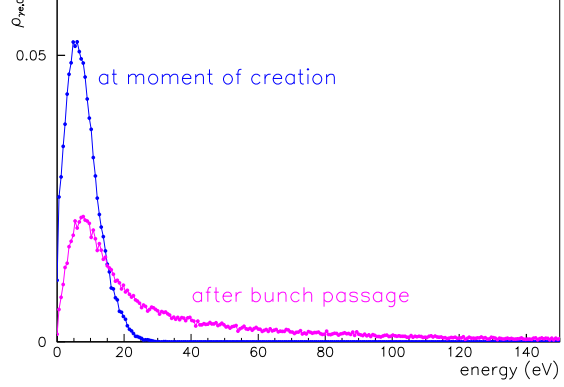Figure 6: Initial photoelectron energy distribution at the moment of emission and after the first bunch passage, for an LHC dipole.

$$B_z(x,y,z) \quad = \quad B_{z0} + B_0 \sin kz .$$

Supposing that the field B_z is sinusoidal, on axis the exact field components follow from Maxwell's equations as [14]

$$B_z(r,z) \quad = \quad B_0 I_0(kr) \cos kz \qquad (2)$$

$$B_r(r,z) \quad = \quad B_0 I_1(kr) \sin kz .$$

Expanding the Bessel functions to first order in radius r, this reduces to the previous formulae.

Further extensions are possible and more than one Fourier component can be kept in the longitudinal field expansion to characterize the more realistic case of a periodic array of solenoids of finite length. Field expressions for this situation were derived by E. Perevedentsev. They read [14]

$$B_r \quad = \quad B_0 \frac{2ka}{\pi} \sum_{n=1}^{\infty} \sin nkh \; K_1(nka) \, I_1(nkr) \; \sin nkz \quad (3)$$

$$B_z \quad = \quad B_0 \left(\frac{2h}{L} + \right.$$
$$\left. \frac{2ka}{\pi} \sum_{n=1}^{\infty} \sin nkh \; K_1(nka) \, I_0(nkr) \; \cos nkz \right) , \quad (4)$$

where the I and K are modified Bessel functions of the first order, a is the solenoid radius, h the solenoid length, L the distance between adjacent solenoids with equal polarity, and B_0 a normalization constant, roughly equal to the field on axis inside the solenoid. in the simulation, the infinite series is truncated at some order, $e.g.$, $n = 5$–50. A similar formula, with odd harmonics doubled and even harmonics set to zero, describes the case of solenoids with alternating polarity, separated by $L/2$. All these expressions

are implemented in ECLOUD and were used for example in simulations for the KEK B factory [15].

The electron motion in field-free region is simply a drift, between kicks (step changes in momentum) representing the effect of the beam field, the electron space charge, and the image charges. For the LHC we often consider a strong dipole, for which we freeze the horizontal and longitudinal position and only consider momentum transfer and electron motion in the vertical direction. This approximation is motivated by the high cyclotron frequency (many cyclotron oscillations per bunch length), namely

$$\omega_c = \frac{eBc}{m_e c^2} \frac{2\sigma_z}{2\pi} \approx 120 \tag{5}$$

for the LHC at 7 TeV ($B = 8.4$ T), and by the small Larmor radius r_L of 6μm for an electron energy of 200 eV. The situation is sketched in Fig. 7. The initial momentum components transverse to the vertical direction are however taken into account in the simulation, namely, when we compute the impact angle on the chamber wall. The angle of incidence modestly influences the secondary emission yield.
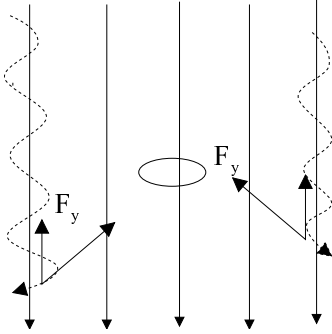

Figure 7: Schematic view of electron motion in a strong vertical dipole field.

For other fields (*e.g.*, 'weaker' dipoles, quadrupoles, solenoids) we use a Runge-Kutta integration. The user can choose between two different Runge-Kutta integrators, taken from the CERN library or the NAG library, respectively.

2.5   Beam and Image Fields

Beam fields are calculated using the standard expression à la Bassetti-Erskine [16] or the simpler formula for round beams. An elegant expression for the field at large distances from a line charge which includes the image charges in an elliptical conducting chamber was given by M. Furman [17]. Denoting by $\mathcal{E} = \mathcal{E}_x + i\mathcal{E}_y$ the complex electric field, Furman's expression reads [17]

$$\mathcal{E} \quad \approx \quad \frac{2}{\bar{z} - \bar{z}_0} + \frac{4}{g} \sum_{n=1}^{\infty} e^{-n\mu_c} \left[\frac{\cosh n\mu_0 \cos n\phi_0}{\cosh n\mu_c} + \right.$$
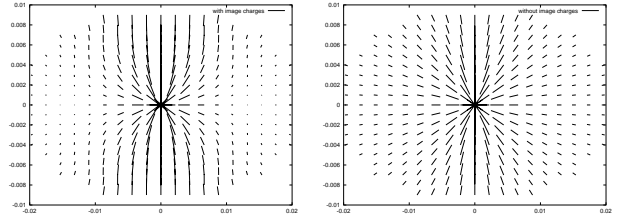

Figure 8: Electric field pattern for a beam centered in an elliptical chamber with [left] and without [right] image charges.
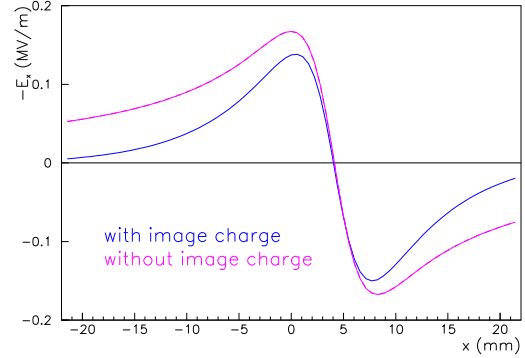

Figure 9: Horizontal electric beam field vs. horizontal position at $y = 0$ for an elliptical chamber with 22×10 mm half apertures and a beam offset of 4.3 mm in both transverse planes.

$$\left. i\, \frac{\sinh n\mu_0 \sin n\phi_0}{\sinh n\mu_c} \right] \frac{\sinh n\bar{q}}{\sinh \bar{q}} \tag{6}$$

where $z = x + iy = g \cosh q = g \cosh(\mu + i\phi)$ denotes the test position, $z_0 = x_0 + iy_0 = g\cosh q_0 = g\cosh(\mu_0 + i\phi_0)$ the position of the source, and both $g = \sqrt{a^2 - b^2}$ and $\mu_c = \tanh^{-1}(b/a)$ characterize the vacuum chamber with semi-axes a and b. In the simulation, the infinite sum is truncated at order $n = 30$.

Figure 8 shows the beam field lines in an elliptical chamber calculated with and without the beam image charges. Figures 9 and 10 depict the horizontal and vertical electric fields for an offset beam as a function of horizontal position, again with and without including the field from the image charges. All three figures demonstrate that the image charges can significantly alter the electron motion.

Image charges of the electron cloud can also be taken into account. The electron charges are assigned to points on a grid, typically consisting of 20×20 or 25×25 points, and the image forces are evaluated for each of the grid points. An example of the electron-cloud self field with and without image charges is shown in Fig. 11.

The minimum number of slices required to accurately model a bunch passage can be determined by considering the motion of electrons with different start positions.
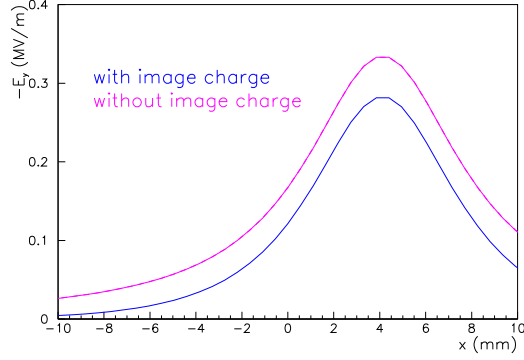
Figure 10: Vertical electric beam field vs. horizontal position at $y = 0$ for an elliptical chamber with 22×10 mm half apertures and a beam offset of 4.3 mm in both transverse planes.
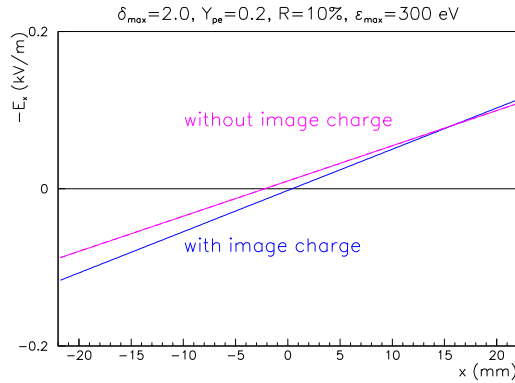

Figure 11: Horizontal electric space-charge field of electron cloud vs. horizontal position after the passage of 8 bunches in the LHC. Parameters: $\delta_{\max} = 2.0$, $Y_{pe} = 0.2$, $R = 0.1$, $\epsilon_{\max} = 300$ eV.

Electrons at large amplitudes do not move much during the bunch passage and simply receive a kick. Electrons near the bunch oscillate in the beam potential. This is shown in Fig. 12. The two amplitude regimes have been called the 'kick region' and the 'autonomous region', respectively, by S. Berg [18].

Hence, it is not surprising that the energy gain of an electron also varies with its initial amplitude. The energy gain further depends on the longitudinal bunch profile. Figure 13 shows a calculation for three different bunch distributions [18]. At the LHC, the maximum possible energy gain is about 2 keV.

2.6 Secondary Emission

Typical measured energy spectra of the emitted secondary electrons are shown in Fig. 14. The figure reveals that the
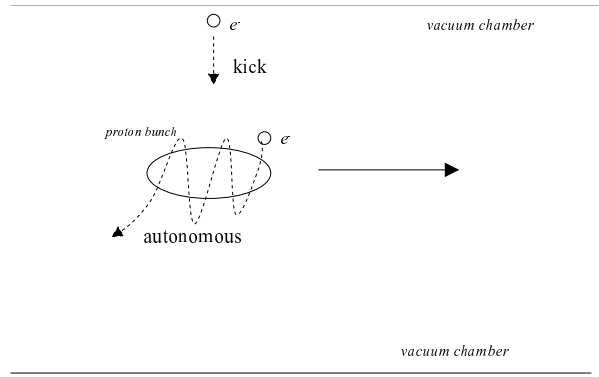

Figure 12: The electron motion during a bunch passage differs qualitatively, depending on the initial position [18].
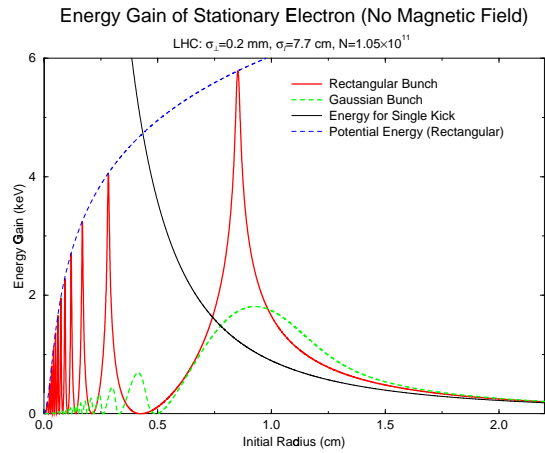

Figure 13: Maximum energy gain of an electron vs. initial particle radial position for nominal LHC parameters [18].

energy spectrum consists of three components: true secondaries with an energy of a few eV, elastically reflected whose energy equals the energy of the incident particle, and rediffused (*i.e.*, the remaining electrons, at intermediate energies).

The relative magnitude of these three components depends on the incident energy. In our simulations with ECLOUD, we presently only distinguish between elastically reflected and true secondaries. The total yield is taken to be the sum of these two components,

$$\delta_{\mathrm{se}} = \delta_{\mathrm{tse}} + \delta_{\mathrm{el}} , \qquad (7)$$

where δ_{tse} denotes the yield of true secondaries and δ_{el} the yield of elastically reflected. Both are functions of the primary-electron energy E and angle of incidence with respect to the surface θ (this θ is not the same as the angle θ of Fig. 4). The elastically reflected electrons are particularly important for small incident energies. There the true yield becomes negligible, whereas for decreasing primary energy the elastic yield converges against a finite value between 30 and 60%. As a consequence, low-energy electrons hitting
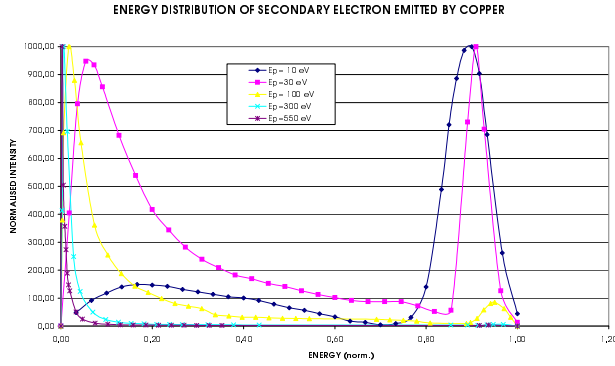
ENERGY DISTRIBUTION OF SECONDARY ELECTRON EMITTED BY COPPER

Figure 14: Normalized secondary electron energy distribution for conditioned copper, revealing three components: true secondaries ($E \ll E_p$), elastically scattered ($E \approx E_p$) and rediffused (in between) [19].

the wall (which are the majority), are not lost, but reflected with a rather high probability, and then can survive until they are accelerated by the next bunch passing by. Thereby the inclusion of elastic reflection results in an increase of the simulated LHC heat load by a factor 2–3 [20].

The actual representation of δ_{el} and δ_{tse} is based on a parametrization of measurements provided by the CERN LHC Vacuum group [19].

According to Furman [10], Seiler [21] and Kirby [22] the yield for the true secondaries can be written

$$\delta_{\mathrm{tse}}(E_{\mathrm{p}}, \theta) = \delta_{\max} 1.11\, x^{-0.35} \left(1 - e^{-2.3 x^{1.35}} \right) \\ \exp\left(0.5\left(1 - \cos\theta \right) \right) , \quad (8)$$

where $x = E_{\mathrm{p}}\left(1 + 0.7(1 - \cos\theta)\right)/\epsilon_{\max}$ [10].

An alternative expression for the true secondaries was proposed by M. Furman [10]:

$$\delta_{\mathrm{tse}}(E_{\mathrm{p}}, \theta) = \delta_{\max} \frac{s \times x}{s - 1 + x^s} \exp\left(0.5\left(1 - \cos\theta\right) \right) , \quad (9)$$

and x is defined as above.

In 2002, we replaced formula (8) by (9), using $s = 1.35$ (this is the value measured for fully conditioned copper; prior to conditioning one finds $s = 1.39$ [19]).

The yield of the true secondaries is then characterized by only two free parameters: $\delta_{\max}$ and $\epsilon_{\max}$. These specify the energy $\epsilon_{\max}$ for which the (true) secondary emission yield is maximum and the value of the maximum yield for perpendicular incidence, $\delta_{\max}$.

The yield of the elastically reflected electrons is written

$$\delta_{\mathrm{el}}(E_{\mathrm{p}}) = f \delta_{\mathrm{se}}(E_{\mathrm{p}}, \theta) , \quad (10)$$

where f was obtained from recent measurements on copper [19], which were fitted to the expression

$$f = \exp\left(A_0 + A_1 \ln(E_{\mathrm{p}} + E_0) + A_2 (\ln(E_{\mathrm{p}} + E_0))^2 \\ + A_3 (\ln(E_{\mathrm{p}} + E_0))^3 \right) . \quad (11)$$

Fits were performed over two different energy ranges. For $E_{\mathrm{p}} \le 300$ eV, the fitted coefficients are [19] $A_0 = 20.7$, $A_1 = -7.08$, $A_2 = 0.484$, $A_3 = 0$, and $E_0 = 56.9$ eV, while, for $E_{\mathrm{p}} \le 2000$eV, $A_0 = -5.1$, $A_1 = 5.6$, $A_2 = -1.62$, $A_3 = 1.1 \times 10^{-5}$, and $E_0 = 29$ eV. Again, all these functions are implemented in the code ECLOUD.

The total secondary emission yield so obtained is illustrated in Fig. 15. For comparison, earlier models without any elastic reflection (in 1999) and with a larger elastic component (2000) are also shown. At the ECLOUD'02 workshop it was remarked that even the latest parametrization is not representative, especially at higher energies [23].
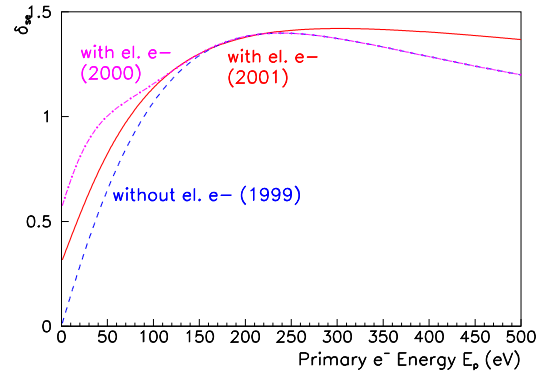

Figure 15: Secondary emission yield for perpendicular incidence vs. primary electron energy with and w/o elastically scattered electrons.

If an electron hits the wall, we determine randomly whether the re-emitted electron represents a true secondary or an elastic electron. More precisely, we choose a random number rand between 0 and 1. If $\mathrm{rand} < f \equiv \delta_{\mathrm{el}}/\delta_{\mathrm{se}}$, we take the electron to be an elastic one; otherwise, if $\mathrm{rand} \ge f$, we treat it as a true secondary.

A recent empirical fit by N. Hilleret [24] of the measured energy spectra for the true secondaries emitted from copper to the formula [25]

$$\rho(E) = C \exp\left[-\frac{(\ln E/E_0)^2}{2\tau^2} \right] \quad (12)$$

yields a good representation of the measurements for $C \approx 0.2$, $E_0 \approx 1.8$ eV, and $\tau \approx 1$ [24]. Equation (12) and its illustration in Fig. 16 show the correct asymptotic behaviour at low energy; namely $\rho(E)$ approaches zero as the energy E goes to zero, a result also expected from phase-space considerations [26]. Previously, the inital energy distribution of the secondary electrons was often taken to be a half Gaussian centered at 0 with rms spread 5 eV, which is also indicated in the figure.

The initial angular distribution of the secondary electrons is taken to be of the form $dN/d\Omega \propto \cos\theta$ [21], which results in $dN/d\theta \propto \sin\theta\cos\theta$, where θ denotes the polar angle with respect to the surface normal. This is illustrated in Fig. 17.
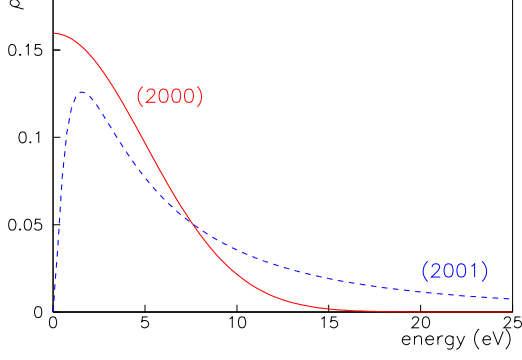
Figure 16: Initial energy spectrum of true secondaries as modelled in 1999/2000 compared with new parametrization by Noel Hilleret [24].
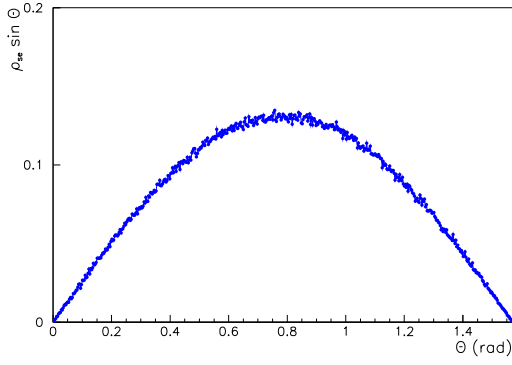

Figure 17: Initial angular distribution $dN/d\theta$ of secondary electrons vs. the polar angle θ with respect to the surface normal.

2.7 Longitudinal Electron Motion

Longitudinal motion of the electrons is included in the simulations. Several effects give rise to this motion [20].

First, the secondary electrons are emitted at an angle θ with respect to the surface normal, following a $\cos\theta$ distribution. Projecting onto the longitudinal direction, we estimate $<\theta_z^2> \approx 0.37\,\mathrm{rad}^2$. The typical longitudinal velocity at emission is

$$v_{z,\mathrm{em}} \approx c \left(\frac{2}{m_e c^2} <\theta_z^2> E_{\mathrm{rms}} \right)^{1/2} \qquad (13)$$

where $E_{\mathrm{rms}} \approx 5$ eV is the rms emission energy. This evaluates to $v_{z,\mathrm{em}} \approx 10^6\,\mathrm{ms}^{-1}$.

For the LHC, a second contribution comes from the magnetic field of the beam. If the electron is initially at rest, its longitudinal velocity after the bunch passage is [28]

$$v_{z,\mathrm{mag}} \approx \frac{1}{2} \frac{v_\perp^2}{c} \approx \frac{\Delta E_{\mathrm{max}}}{mc} \approx \frac{2cN_b r_e}{\sqrt{2\pi}\sigma_z} \log \frac{r_c}{c_0 \sigma_\perp} \qquad (14)$$

where $c_0 \approx 1.06$, and [18]

$$r_c \approx 2\sqrt{N_b r_e \sigma_z \sqrt{2/\pi}} \qquad (15)$$

Inserting the LHC parameters, we find $r_c \approx 8.5$ mm (this is the critical radius separating the kick approximation and the autonomous region [18]), and $v_{e,\mathrm{mag}} \approx 3 \times 10^6\,\mathrm{ms}^{-1}$. Simulations show that for LHC the electron energy gain ΔE_{max} is about a factor 3 smaller than predicted by the above analytical approximation. Therefore, a more realistic estimate is $v_{e,\mathrm{mag}} \approx 10^6\,\mathrm{ms}^{-1}$, which is comparable to the longitudinal emission velocity. This order of magnitude was confirmed by simulations [27].

However, in a strong dipole field both the beam magnetic field and the emission velocity can be neglected. In this case, the electrons undergo a rapid cyclotron oscillation. Superimposed is a uniform longitudinal motion ($\vec{E} \times \vec{B}$ drift). We estimate the maximum drift velocity encountered during the bunch passage as

$$v_{e,\mathrm{drift}} \approx \frac{N_b e}{\sqrt{2\pi}\sigma_z 4\pi\epsilon_0(\sigma_x + \sigma_y)B} \,, \qquad (16)$$

where B is the dipole magnetic field. For the LHC parameters, we obtain $v_{e,\mathrm{drift}} \approx 1.6 \times 10^5\,\mathrm{ms}^{-1}$.

A quadrupole magnet also causes a 'gradient drift' at a velocity equal to

$$v_{e,\mathrm{gradient}} = \frac{r_L^2 \omega_c}{2} \frac{(\vec{\nabla}\vec{B}) \times \vec{B}}{B^2} \,, \qquad (17)$$

where $r_L = p_e/(eB)$ is the Larmor radius and $\omega_c = eB/m_e$ the (non-relativistic) cyclotron frequency. Using $\vec{B} = 200$ T/m, $B = 2$ T (i.e., considering an electron at amplitude 1 cm), and a typical electron energy of 100 eV, we obtain $v_{e,\mathrm{gradient}} \approx 5 \times 10^3\,\mathrm{ms}^{-1}$.

Thus, in a field-free region we expect longitudinal electron motion at a typical speed of a few $10^6\,\mathrm{ms}^{-1}$, whereas in an 8.4-T dipole field the maximum longitudinal velocity does not exceed $2 \times 10^5\,\mathrm{ms}^{-1}$. The average drift velocity in a dipole is even lower by a factor 50, because the beam is absent most of time. Finally, the gradient drift in a quadrupole of about $5 \times 10^3\,\mathrm{ms}^{-1}$ may be comparable to the average drift in a dipole.

Our estimates are confirmed by simulations for field-free regions and dipoles, as is illustratred in Fig. 18.

The relatively low longitudinal speed implies that electrons are lost transversely to the wall before they can traverse a longitudinal distance comparable to the magnet dimensions. This provides a justification why we may separately simulate the electron cloud build up for regions of different magnetic fields without taking into account any electron exchange between those regions.
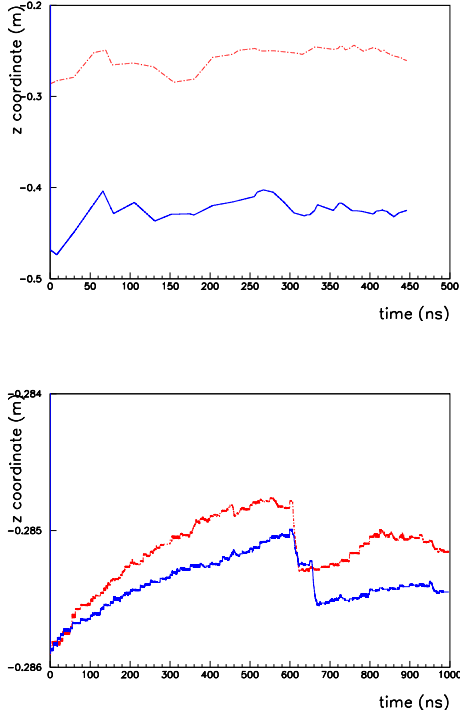
Figure 18: Longitudinal coordinate versus time for two sample electron trajectories in a field free region (top) and in a 1-T dipole field (bottom).

3 EXAMPLE RESULTS

3.1 Electron Cloud Build-Up in Dipoles and Field-Free Regions, Energy Spectrum

Figure 19 shows the simulated build up of an electron cloud for a field-free region and for a dipole field in the CERN SPS. The chamber dimensions are assumed to be the same in the two cases, with $h_x = 76$ mm, and $h_y = 17.5$ mm (flat geometry). The various curves refer to different bunch intensities. The figure demonstrates that in the dipole field significant electron build up starts at a lower bunch intensity, although at higher intensities the cloud can reach larger densities in the field-free region. The lower threshold for the dipole field is attributed to the flatness of the chamber. The 'overshoot' before saturation that is visible for the field-free region appears to be related to the elastically reflected electrons.

Simulations were also performed for the SPS fixed target beam. This beam consists of 2 trains of about 2100 bunches with a bunch spacing of 5 ns, a train-to-train spacing of 1.05 μs and a single-bunch intensity N_b below 10^{10} protons per bunch. Figure 20 compares the simulated electron cloud build for $N_b = 5 \times 10^9$ and $N_b = 7 \times 10^9$, considering a maximum secondary emission yield of $\delta_{max} = 1.8$. No build up is observed for the lower bunch intensity, but a significant build up occurs in the second case. Thus, the sim-
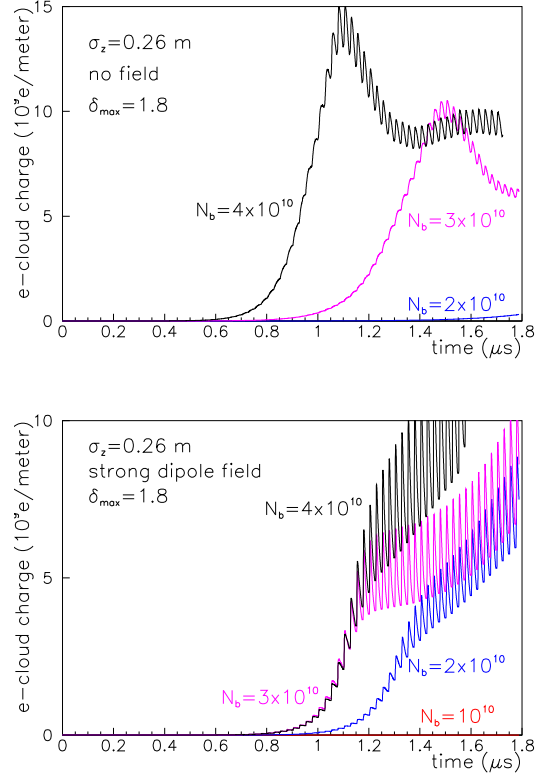

Figure 19: Simulated electron-cloud build up in the SPS for a field-free region (top) and a strong dipole (bottom), comparing various bunch populations. In field-free regions threshold is higher, but the build up above the threshold stronger.

ulated threshold of electron amplification due to multipacting is about $N_b \approx 6 \times 10^9$, which is roughly consistent with observations [29]. In these simulations, we have assumed the measured rms transverse beam sizes of $\sigma_x = 1.2$ mm and $\sigma_y = 0.7$ mm, and an rms bunch length of $\sigma_z = 0.1875$ m. All these numbers are considerably smaller than for the LHC type beam, which explains why the multipacting here occurs for smaller bunch intensity.

In Sect. 2 we mentioned that the motion of electrons in a dipole field can be modelled in different ways. For example, in one approach, we ignore the horizontal and longitudinal motion, in the other we employ a library Runge-Kutta integration. Figure 22 compares the simulated electron build up computed by these two approaches for a 0.26-T field in the KEKB High Energy Ring. The agreement is quite reasonable, even for a field as low as this.

3.2 Multibunch Wake

The electron cloud couples the motion of subsequent bunches. A displaced bunch disturbs the symmetry of the cloud, and the following bunch receives a net deflection. This effect is illustrated in Fig. 23 for an LHC bunch train.
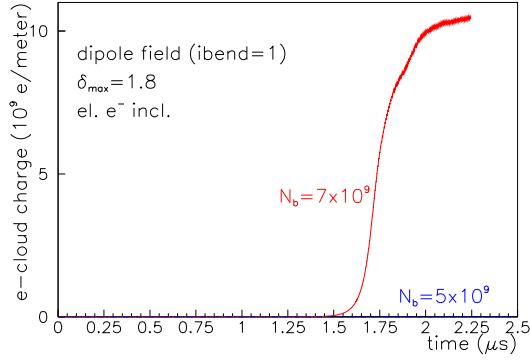
Figure 20: Electron-cloud line density vs. time in a dipole field for the SPS fixed-target beam with 5-ns spacing.
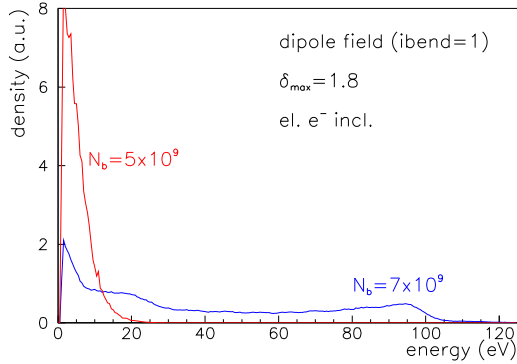

Figure 21: Energy spectrum of electrons hitting the wall in a dipole field for the SPS fixed-target beam with 5-ns spacing, comparing two different bunch intensities.
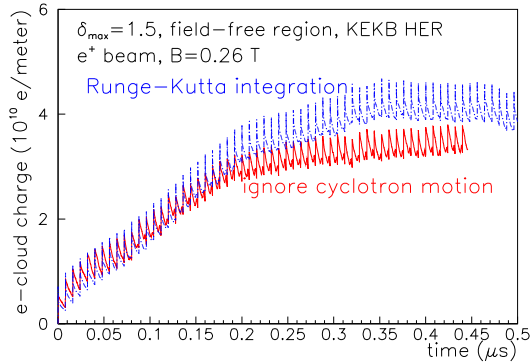

Figure 22: Electron-cloud line density vs. time in a 0.26-T dipole field for an positron beam in the KEKB HER comparing two different models of electron motion.

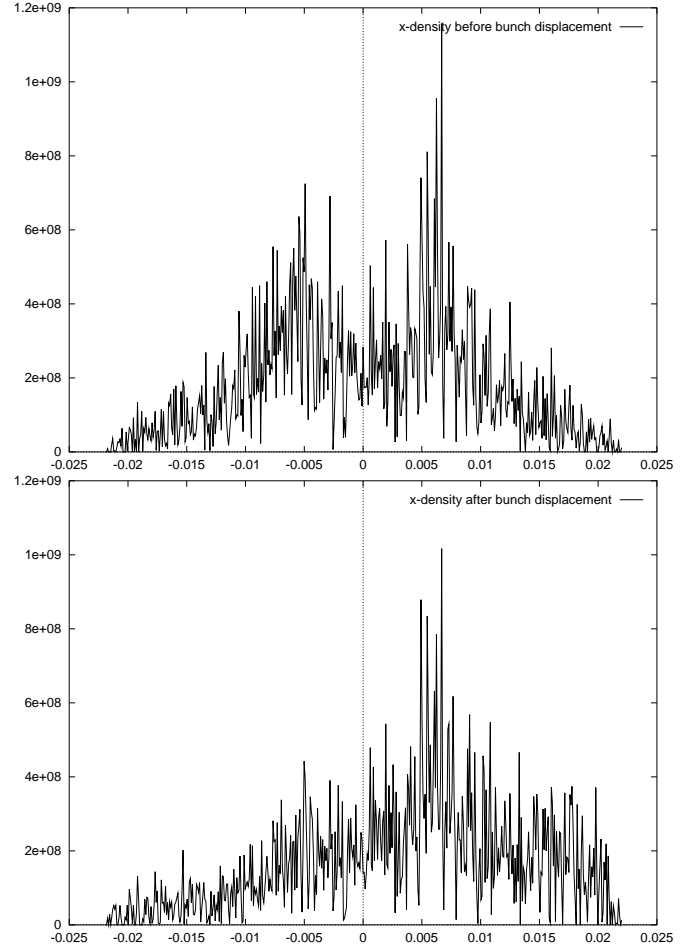Thus, similar to a multibunch wake field, the electron cloud couples the motion of subsequent bunches.

Figure 23: Projected horizontal electron charge density in an LHC bending magnet before the 41st bunch in the train is horizontally displaced by 1 cm (top) and just prior to the arrival of the 42nd buncha (bottom) [4]. The horizontal axis is in units of meters; the vertical coordinate is the charge (in units of e) per bin and per grid point. Other parameters: 500 grid points, $\delta_{\max} = 1.7$, $R = 1$, $Y^* = 1$.

The ECLOUD programme computes the effective wake field as follows. After a stationary cloud is established, one of the bunches is displaced transversely by an amount Δx or Δy. Then, we calculate the kick that the disturbed e^- cloud exerts on the next bunch. This yields an estimate of the bunch-to-bunch dipole wake field $W_1(L_{sep})$ [31, 10, 1]:

$$W_1(L_{sep}) = \sum_i \frac{2y_i Q_i}{N_b r_i^2 (\Delta y)} \left(1 - \exp\left(-\frac{r_i^2}{2\sigma^2} \right) \right) \frac{C}{l_b},$$
(18)

where $r_i = (x_i^2 + y_i^2)^{1/2}$ (the radial distance of the ith macro-electron from the beam axis), C is the ring circumference, l_b is the simulated length of bending magnet, and Q_i denotes the charge of the ith macro-electron.

The bunch-to–bunch wake field can give rise to a multi-bunch instability. From the wake field acting between successive bunches, we can estimate the instability growth time. To obtain this growth rate, we assume that the ring is uniformly filled with M bunches and that the wake of the electron cloud decays rapidly and only couples subsequent bunches. Then the complex frequency shift of μth mode is given by [30]

$$\Omega_{y\ (x)}^{(\mu)} - \omega_{\beta,y\ (x)} = \frac{N_b r_p c^2}{2\gamma C \omega_\beta} W_{1,y\ (x)} e^{i2\pi(\mu+Q_{y\ (x)})/M} \tag{19}$$

and the rise time for the fastest growing mode is

$$\tau \approx \frac{4\pi\gamma Q_{y\ (x)}}{N_b r_p c W_{1,y\ (x)}} \tag{20}$$

If the ring is not uniformly filled and there are clearing gaps, the growth is not exponential but

$$y_n \sim \frac{1}{n!}(t/\tau)^n \,\hat{y}_0 \tag{21}$$

for the nth bunch in a train. It was pointed out by M. Furman [31] that the parameter τ is exactly the same as the exponential growth time for the uniform fill, which was given above.

Simulated horizontal and vertical multi-bunch instability growth rates for the LHC at 7 TeV are shown in Fig. 24 as a function of the maximum secondary emission yield $\delta_{\max}$. The instability is slow, with rise times longer than 1 second. We expect that it is Landau damped by the natural intra-bunch tune spread.
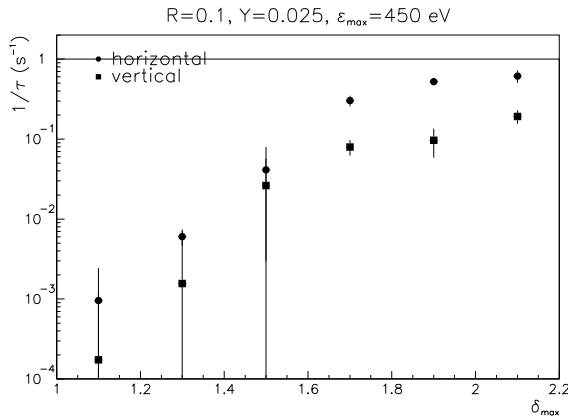

Figure 24: Multibunch instability growth rate as a function of maximum secondary emission yield $\delta_{\max}$ for the LHC at 7 TeV [4]. Other parameters: $\epsilon_{\max} = 450$ eV, $R = 10\%$, and $Y_{pe} = 0.025$.

3.3 Effect on Beam Diagnostics

The impact of the electron cloud on the reading of LHC beam-position monitors (BPMs) was studied in Ref. [5].

Figure 25 shows a schematic of a BPM in the LHC arc. The direct synchrotron radiation hits the horizontally outward electrode. Photoelectrons are emitted primarily from this electrode, which results in a net flow of electrons to the other 3 BPM buttons.
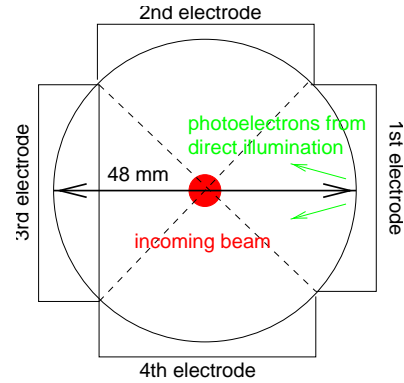

Figure 25: Schematic cross section of a BPM in the LHC arc [5]. Length of the device is 24 mm. Direct synchrotron radiation illuminates the first electrode.

Figure 26 shows a simulation result for the electron current on the four electrodes, experienced during the passage of an LHC batch [5]. It illustrates the continuous loss of electrons from the first to the other three electrodes. At larger values of $\delta_{\max}$ (bottom picture), a random component due to multipacting is added to the average current flow determined by the synchrotron radiation.

Figure 27 illustrates the time and frequency structure of the electron current at one of the electrodes [5]. The electron signals peak during the bunch passages, and the frequency spectrum roughly images the bunch frequency contents.

The response the BPM processing electronics to the simulated input signal was studied independently by R. Jones [32]. He found that the reading error induced by the electron cloud is quite small, of the order of 2 μm [32].

3.4 Spatial Structure of the Electron Cloud

In a LHC or SPS dipole magnet, at sufficiently high bunch charges the cloud consists primarily of two vertical strips located on either side of the beam. These stripes are attributed to the maximum in the secondary emission yield curve. Electrons in the strip region aquire a typical energy close to this maximum. In 2001 a dedicated monitor was installed in the SPS which directly demonstrated the existence of the two strips at sufficiently high current [33].

Figure 28 shows the simulated flux of electrons on the chamber wall for SPS parameters. In this simulation the primary electrons (thought to be due to beam loss or gas ionization) were launched at the chamber wall, uniformly distributed as a function of azimuthal energy. For higher bunch charges, two strips exist, located symmetrically about the position of the beam (only the right-hand
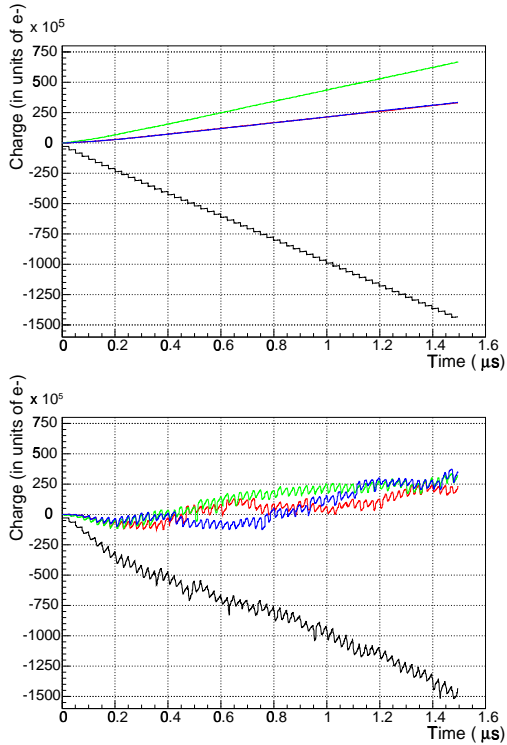
Figure 26: Net charge deposited or emitted at each BPM electrode for $\delta_{\max} = 1.1$ (top) and $\delta_{\max} = 1.9$ (bottom) [5]. Negative values indicate that a net flow of electrons away from the plate.
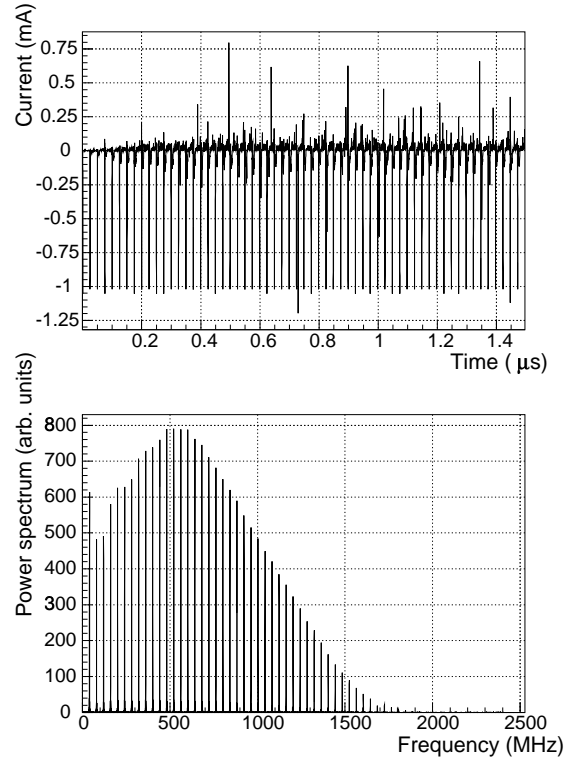

Figure 27: Instantaneous electron current at the first electrode vs. time (top) and its power density spectrum vs. frequency (bottom) for a maximum secondary emission yield $\delta_{\max} = 1.5$ [5]. In the top picture, the large negative spikes which coincide with bunch passages represent the primary photoemission. In the bottom picture, the fall-off of the signal power spectrum occurs near the bunch frequency $f_{\text{bunch}} = c/(2\pi\sigma_z) \approx 700$ MHz.

side is shown). At $N_b = 8 \times 10^{10}$ in the simulation there is even evidence for a third strip emerging again at the center of the chamber.

Figure 29 compares simulation results where in the first case the electrons are launched at the wall, and in the second inside the beam volume in order to more accurately model the gas ionization by the beam. The spatial structure is clearly different in the two cases. In particular, the vertical strips cannot build up in the second case, because no primary electrons are present at their horizontal location. This figure also demonstrates the effect of changing the value of $\epsilon_{\max}$, i.e., the incident energy where the secondary emission yield assumes a maximum value. Each curve corresponds to a different $\epsilon_{\max}$. For lower values of $\epsilon_{\max}$ the strips move outwards, and, in addition, the electron flux increases strongly.

Despite of the difference in the spatial structure, the total number of electrons and their build-up time are quite similar for these two cases, as is illustrated in Fig. 30.

Finally, Fig. 31 shows the simulated electron cloud distribution in an LHC quadrupole magnet. The cloud exhibits a fourfold symmetry corresponding to the symmetry of the magnetic field. Strong multipacting and heat load deposition primarily occur along the diagonals at $45°$, which pass through the center of the chamber [36]. In the other regions, electrons might become trapped in the magnetic

field [37]. This aspect will be addressed in the next section.

3.5 Electron Trapping in Quadrupoles

It was first discovered in simulations by L. Wang [37], that after acceleration by the beam electrons can become trapped inside a quadrupole field, like in a magnetic bottle.

Figures 32 and 33 show the simulated build up of electrons during the passage of a 50-bunch train as well as the subsequent decay of the cloud. In the first picture all electric fields are taken into account during the decay; the second picture shows the decay if electrons experience only the magnetic field.

In neither case does the number of electrons shrink to zero, over the time scale considered, raising the possibility that a certain fraction of the electron might remain trapped forever.

In the case without image and space-charge forces, if only the magnetic field is present, the trapping condition
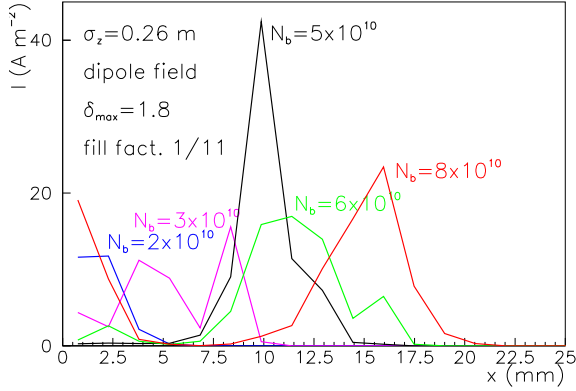
Figure 28: Simulated electron flux on chamber wall in A/m^2 vs. the horizontal position in an SPS dipole, for different values of the bunch population. Simulation parameters: $\sigma_x = 3.5$ mm, $\sigma_y = 1.6$ mm, $\sigma_z = 0.26$ m, $\delta_{\max} = 1.8$, $\epsilon_{\max} = 300$ eV, $d\lambda_e/ds = 2.5 \times 10^{-7}$ m^{-1} per proton, $h_x = 76$ mm, $h_y = 17.5$ mm, $L_{\text{sep}} = 7.48$ m, $B = 0.2$ T; elastic electron reflection included.

is given by [34]

$$T \equiv \frac{v_{\text{tot}}^2 B_{\text{local}}}{v_\perp^2 B_{\text{pipe}}} < 1 \,, \tag{22}$$

where v_{tot} denotes the total velocity of the electron, $f_\perp$ the velocity components transverse to the local magnetic field, B_{local} the local field strength, and B_{pipe} the field at the chamber wall following the magnetic field lines.

Figure 34 displays a histogram of the quantity $\ln(T)$, evaluated for all electrons after the passage of 50 bunches through a KEKB-LER quadrupole. Trapping corresponds to $\log(T) < 0$.

Finally, Fig. 35 depicts the fraction of electrons for which the trapping condition $\log(T) < 0$ is fulfilled as a function of time, for the two cases corresponding to Figs. 32 and 33.

3.6 Electron Cloud Build Up for Electron Beams

For an electron beam and for a positron beam the number of photo-electrons is the same. In the case of the electron beam, the primary photoelectrons, if emitted at the time of the bunch passage, are immediately repelled by the beam field. Therefore, the electron cloud build up should be reduced compared with that for a positron beam.

However, even if the photo-electrons are repelled they might be reflected back from the chamber wall with a high probability. In addition, in the case of one or several photon reflections, the photo-electrons may be emitted after the bunch has completely passed by [39]. Then they do not experience the repelling field of the bunch which generated
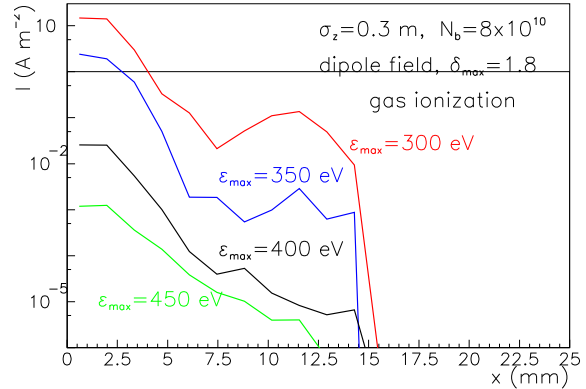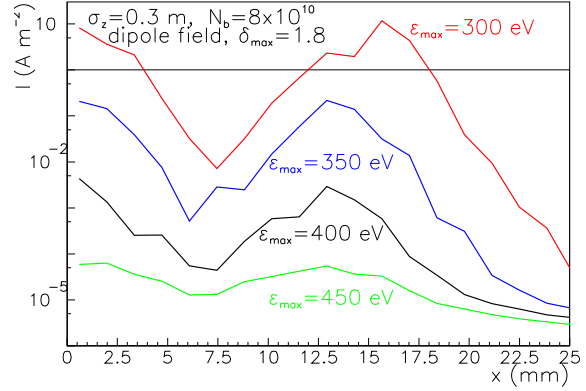

Figure 29: Electron flux on chamber wall in A/m^2 vs. the horizontal position in an SPS dipole for various values of $\epsilon_{\max}$; top: launching primary e$^-$ at the wall; bottom: launching primary e$^-$ inside beam (ionization). Simulation parameters: $\sigma_x = 3.5$ mm, $\sigma_y = 1.6$ mm, $\delta_{\max} = 1.8$, $d\lambda_e/ds = 2.5 \times 10^{-7}$ m^{-1} per proton, $N_b = 8 \times 10^{10}$, $h_x = 76$ mm, $h_y = 17.5$ mm, $L_{\text{sep}} = 7.48$ m, $B = 0.2$ T; elastic electron reflection included.

them. This will happen more easily for electron beams than, e.g.,for anti-proton beams, since the electron bunch lengths are typically much shorter.

In a recent study for the KEKB HER [35] we simulated a worst-case situation where, for the electron beam, all primary photo-electrons were launched just after the passage of the emitting bunch. Figure 36 compares the simulated build up of the electron cloud for the KEKB HER when operated with positron or electron beams of the same current. The total number of electrons differs by a factor of 4 or 5. Therefore, at high beam current we expect to observe electron-cloud effects also for the electron beams. This might be a possible explanation for a fast horizontal coupled-bunch instability which has been observed in the KEKB HER [38, 35].
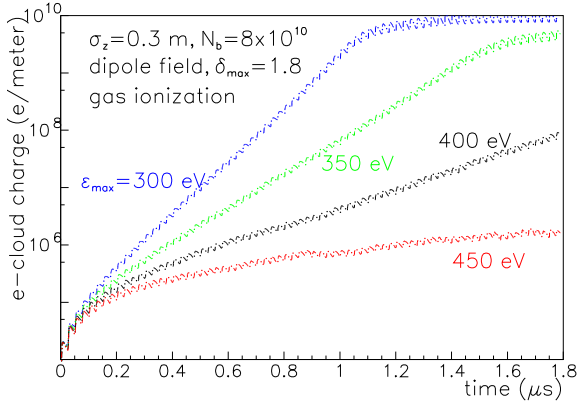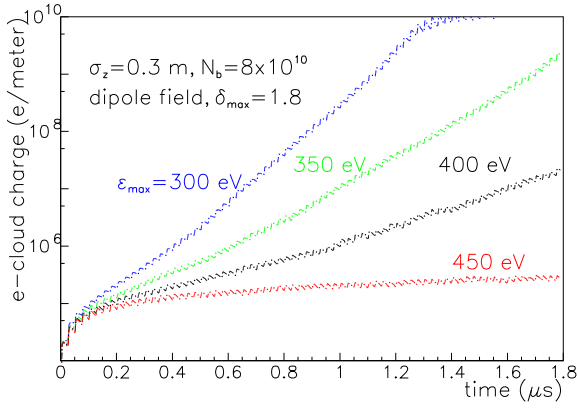
Figure 30: SPS electron line density vs. time for various values of ϵ_{max}; top: launching primary e$^-$ at the wall; bottom: launching primary e$^-$ inside beam (ionization). Simulation parameters: $\sigma_x = 3.5$ mm, $\sigma_y = 1.6$ mm, $\delta_{max} = 1.8$, $d\lambda_e/ds = 2.5 \times 10^{-7}$ m^{-1} per proton, $N_b = 8 \times 10^{10}$, $h_x = 76$ mm, $h_y = 17.5$ mm, $L_{sep} = 7.48$ m, $B = 0.2$ T; elastic electron reflection included.
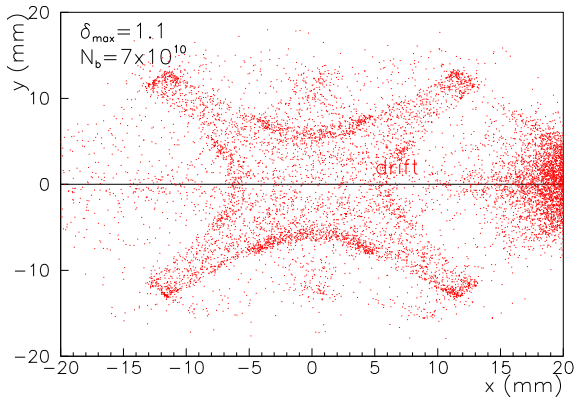

Figure 31: Snapshot of transverse electron distribution in an LHC quadrupole chamber. Parameters: $\delta_{max} = 1.1$, $N_b = 7 \times 10^{10}$.
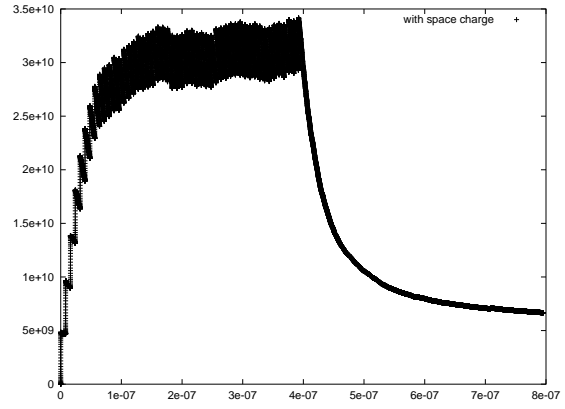

Figure 32: Simulated electron line density vs. time for a quadrupole field in the KEKB LER [35]; this simulation includes electron space-charge and image fields.
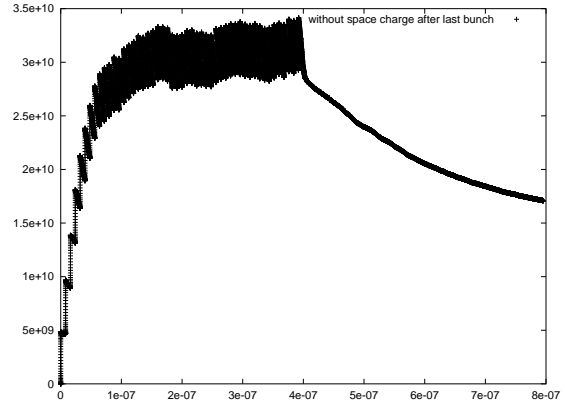

Figure 33: Simulated electron line density vs. time for a quadrupole field in the KEKB LER [35]; in this simulation electron space-charge and image fields are switched off after the passage of the last bunch, from which time onwards the electrons only experience magnetic forces.
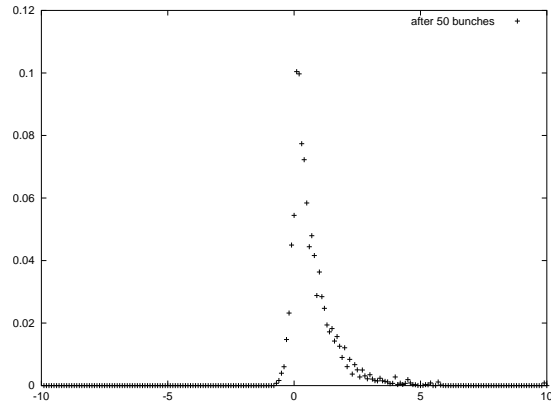

Figure 34: Histogram of simulated electron trapping parameter $\log(T)$ after the passage of 50 bunches for a quadrupole field in the KEKB LER [35].
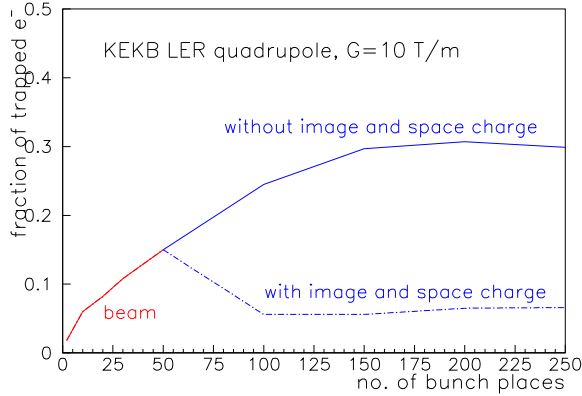
Figure 35: Fraction of electrons for which $\log(T) < 0$ (*i.e.*, for which the trapping condition is fulfilled) as a function of bunch-space number [35]. The beam stops after 50 bunches.
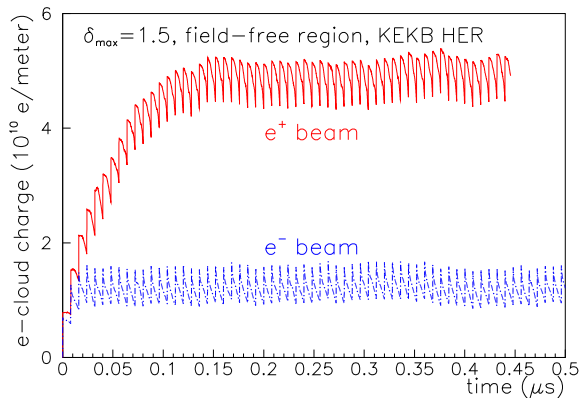

Figure 36: Electron-cloud line density vs. time in a 0.26-T dipole field for the KEKB HER comparing electron beam and positron beams [35].

4 CONCLUSIONS

Simulations of electron-cloud build up and heat load (for LHC) are sensitive to the parametrization of secondary emission and photoemission. Important are also the beam and electron image charges, the electron space charge, and magnetic fields, even if they are only a few Gauss.

The simulated electron-cloud build up is in good agreement with observations for the CERN SPS, the CERN PS [40], and the KEKB LER.

The largest remaining discrepancy between SPS measurements and simulations pertains to the exact position of the vertical stripes in an SPS dipole. The present difference is about a factor of two for a bunch population of $N_b \approx 8 \times 10^{10}$, the simulation predicting a larger distance between the strips and the beam axis. It is conceivable that

this discrepancy can be resolved by a different parametrization of the secondary emission yield [41].

Simulations with the code ECLOUD confirm that a certain fraction of electrons, between 5% and 30%, may be trapped inside a quadrupole field. This corroborates previous simulation results by L. Wang [37], though the exact fraction of trapped electrons might still be different.

Finally, our simulations suggest that a significant electron cloud can also build up for an electron beam. This was illustrated with an example for the KEKB HER.

5 ACKNOWLEDGEMENTS

6 REFERENCES

[1] F. Zimmermann, "A simulation study of electron-cloud instability and beam-induced multipacting in the LHC", LHC Project-Report 95, and SLAC-PUB-7425 (1997).

[2] O. S. Brüning, "Simulations for the beam-induced electron cloud in the LHC beam screen with magnetic field and image charges," CERN LHC PR 158 and EPAC98 (1997).

[3] F. Ruggiero and X. Zhang, "Collective Instabilities in the LHC: Electron Cloud and Satellite Bunches," in Proc. Workshop on Instabilities of High Intensity Hadron Beams in Rings, BNL, 28 June-1st July 1999, AIP Conf. Proceedings 496, pp. 40-48 (1999).

[4] F. Zimmermann, "Electron-Cloud Simulations for SPS and LHC", Chamonix X, CERN-SL-2000-007 (2000).

[5] G. Rumolo et al., "Simulation of the Electron-Cloud Build Up and Its Consequences on Heat Load, Beam Stability and Diagnostics," PRST-AB 012801 (2001).

[6] G. Rumolo, F. Zimmermann, "Electron-Cloud Simulations," Proc. Int. Workshop on Two-Stream Instabilities, KEK, Tsukuba, September 2001 (2001); in CERN SL-2001-067 (AP).

[7] G. Rumolo and F. Zimmermann, "Practical User Guide for ECloud," CERN SL-Note-2002-016 (AP) (2002).

[8] G. Rumolo, F. Zimmermann, programme documentation at *http://wwwslap.cern.ch/collective/electron-cloud/electron-cloud.html*

[9] M.A. Furman, G.R. Lambertson, "The Electron Cloud Instability in PEP-II: An Update," IEEE PAC 97, Vancouver (1997).

[10] M.A. Furman and G.R. Lambertson, "The Electron Cloud Effect in the arcs of the PEP-II Positron Ring," KEK Proceedings 97-17, p. 170, December 1997 (Proc. MBI97 workshop, KEK, Y.H. Chin, ed.) (1997).

[11] F. Zimmermann, "The Electron Cloud Instability: Summary of Measurements and Understanding," Proc. PAC'2001 Chicago, USA, CERN-SL-2001-035 (AP) (2001).

[12] F. Zimmermann, "Electron-Cloud Effects in the LHC," presented at ECLOUD'02, Geneva April 2002 (2002).

[13] I. Collins, private communcation (2000).

[14] E. Perevedentsev, "Periodic Solenoid Field", unpublished note, KEK, November 2000.

[15] F. Zimmermann, H. Fukuma, and K. Ohmi, "More Electron Cloud Studies for KEKB: Long-Term Evolution, Solenoid Patterns, and Fast Blow Up," CERN-SL-Note-2000-061 AP (2000).

[16] M. Bassetti and G. A. Erskine, "Closed Expression For The Electrical Field Of A Two-Dimensional Gaussian Charge," CERN-ISR-TH/80-06 (1980).

[17] M. Furman, "Comments on the Electron-Cloud Effect in the LHC Dipole Bending Magnets", KEK Proceedings 97-17, p. 234, December 1997 (Proc. MBI97 workshop, KEK, Y.H. Chin, ed.) (1997).

[18] J.S. Berg, "Energy Gain in an Electron Cloud during the Passage of a Bunch", LHC Project Note 97 (1997).

[19] V. Baglin, I. Collins, B. Henrist, N. Hilleret, G. Vorlaufer, "A Summary of the Main Experimental Results Concerning the Secondary Electron Emission of Copper," LHC-Project-Report-472 (2001).

[20] F. Zimmermann, "Electron-Cloud Simulations: An Update", Chamonix XI, CERN-SL-2001-003-DI (2001).

[21] H. Seiler, "Secondary electron emission in the scanning electron microscope", J. Appl. Phys. 54 (11) (1983).

[22] R. Kirby, et al., "Secondary Electron Emission from Accelerator Materials," Proc. 8th ICFA Beam Dynamics Mini-Workshop on Two-Stream Instabilities, Santa Fe (2000); R. Kirby and F. King, "Secondary Electron Emission Yields from PEP-II Accelerator Materials", SLAC-PUB-8212 (2000).

[23] O. Grobner amd N. Hilleret, private communcations at ECLOUD'02 (2002).

[24] N. Hilleret, "An empirical fit to the true secondary electron energy distribution," unpublished draft, dated 23.10.01 (2001).

[25] J.J. Scholtz, D. Dijkkamp, R.W.A. Schmitz, Philips J. Res. 50, 375–389 (1996).

[26] A. Chao, K. Oide, comments at the International Workshop on Two-Stream Instabilities, KEK, September 2001 (2001).

[27] A. Arauzo and F. Zimmermann, "Electron-Cloud Energy and Angular Distributions," CERN-SL-Note-2000-057 AP (2000).

[28] J. Buon, F. Couchot, J. Jeanjean, F. Le Diberder, V. Lepeltier, H. Nguyen Ngoc, J. Perez-y-Jorba, P. Chen, "A Beam Size Monitor for the Final Focus Test Beam," NIM A 306, p. 93 (1991).

[29] G. Arduini, private communication (2001).

[30] A.W. Chao, "Physics of Collective Beam Instabilities in High Energy Accelerators", Wiley (1993).

[31] M. Furman and G. Lambertson, "The Electron-Cloud Effect in the LER: A Status Report," and subsequent discussion during the PEP-II MAC meeting, SLAC, 7 January 1997 (1997).

[32] R. Jones, private communication (2000).

[33] M. Jimenez et al., these proceedings.

[34] private discussion with K. Ohmi, L.Wang, and K. Oide (2002).

[35] F. Zimmermann, "Accelerator Physics Studies for KEKB: Electron Trapping, Electron Cloud in the HER, Closed-Orbit Drift, Horizontal Instability and Tune Shift," CERN SL-Note-2002-017 (AP) (2002).

[36] F. Zimmermann, H. Fukuma, and K. Ohmi, "More Electron-Cloud Studies for KEKB: Long-Term Evolution, Solenoid Patterns, and Fast Blow Up," CERN SL-Note-2000-061 AP (2000).

[37] L. Wang, Proc. Int. Workshop on Two-Stream Instabilities, KEK, Tsukuba, September 2001 (2001).

[38] S.S. Win, H. Fukuma, E. Kikutani, M. Tobiyama, "Observation of Transverse Coupled Bunch Instability at KEKB," APAC01 (2001).

[39] J. Galayda, private communcation, visit at APS, February 1997 (1997).

[40] R. Cappi et al., these proceedings.

[41] O. Grobner commented during the workshop that the parametrization employed may not be representative.